


Cite this: *RSC Adv.*, 2023, 13, 36009

# Combined experimental and simulation study on H<sub>2</sub> storage in oxygen and nitrogen co-doped activated carbon derived from biomass waste: superior pore size and surface chemistry development†

Suphakorn Anuchitsakol,<sup>a</sup> Waralee Dilokekunakul,<sup>b</sup> Numphueng Khongtor,<sup>c</sup> Somboon Chaemchuen<sup>id</sup><sup>d</sup> and Nikom Klomkliang<sup>ib</sup><sup>\*ae</sup>

In this study, heteroatom (O, N)-doped activated carbon (AC) is produced using urea and KOH activation from abundant and cost-effective biomass waste for H<sub>2</sub> storage. The O and N co-doped AC exhibits the highest specific surface area and H<sub>2</sub> storage capacity (2.62 wt%), increasing by 47% from unmodified AC at −196 °C and 1 bar. Surface modification helps develop superior pore sizes and volumes. However, the original AC is superior at lower pressures (<0.3 bar) because of its suitable pore width. This observation is then explained by molecular simulations. Optimal pore widths are 0.65 nm at <0.3 bar and 0.95–1.5 nm at pressures in moderate range (0.3–15 bar). Superior pore sizes are observed in the range of 0.8–1.3 nm at 1 bar, enhancing performance with co-doped AC to achieve uptake superior to that of other ACs described in the literature. However, above 15 bar, pore volume dominates capacity over pore width. Among the O and N groups, pyridinic-N oxide is the most substantial, playing a vital role at low and moderate pressures. These findings propose a strategy for superior H<sub>2</sub> storage in porous carbons under various pressure conditions.

Received 3rd October 2023  
Accepted 27th November 2023

DOI: 10.1039/d3ra06720c

rsc.li/rsc-advances

## 1. Introduction

Global energy demand is surging, with over 78% of the world population reliant on non-renewable fossil fuels according to data from 2023.<sup>1</sup> However, their combustion emits greenhouse gases, contributing to climate change. To address this, innovative technologies for clean and renewable energy, including hydrogen storage, have emerged.<sup>2,3</sup> Hydrogen is an eco-friendly fuel with a high energy content (142 MJ kg<sup>−1</sup>) which is about three fold higher energy per unit mass compared to gasoline,<sup>4</sup> and water is its byproduct. Nevertheless, efficient transport and storage of hydrogen pose challenges. One promising approach is cryogenic storage in porous materials known for their rapid

kinetics, excellent cyclability, and high adsorption capacity.<sup>5,6</sup> Extensive research has focused on activated carbons (ACs),<sup>7–14</sup> metal-organic frameworks,<sup>15–18</sup> and zeolites<sup>19–21</sup> as potential hydrogen storage materials. ACs, in particular, offer advantages such as large surface area, customizable porosity, thermal and chemical stability, affordability, and versatility in raw material sources.<sup>22–24</sup> Modifying ACs with heteroatoms such as oxygen, sulfur, nitrogen, and phosphorus has shown promising results in enhancing surface and pore properties.<sup>25–27</sup>

Numerous studies have investigated the influence of pore size on hydrogen adsorption.<sup>28–32</sup> It has been noted that AC micropores ranging from 0.60 to 0.70 nm and 0.65 to 1.5 nm exhibited optimal hydrogen storage capabilities at −196 °C.<sup>33,34</sup> The surface area played a crucial role in hydrogen adsorption, while the nitrogen or sulfur content in modified ACs did not significantly affect it.<sup>35,36</sup> Adequate pore volume and a large surface area were essential for substantial hydrogen uptake and could compensate for the presence of larger pores (>1.0 nm).<sup>31,33</sup> Furthermore, investigations into the surface chemistry of ACs revealed that a high proportion of carbon surface micropores and oxygen functional groups enhanced gravimetric hydrogen storage efficiency.<sup>37,38</sup> In a recent study, ammonia treatment of a commercial AC improved hydrogen adsorption efficiency from 1.98 to 2.34 wt% at −196 °C and 0.93 bar.<sup>39</sup> However, a separate study concluded that pore width had a more significant impact

<sup>a</sup>School of Chemical Engineering, Suranaree University of Technology, Nakhon Ratchasima 30000, Thailand. E-mail: nikom.klo@sut.ac.th

<sup>b</sup>Aachener Verfahrenstechnik – Chemical Process Engineering, RWTH Aachen University, Aachen 52074, Germany

<sup>c</sup>Institute of Research and Development, Suranaree University of Technology, Nakhon Ratchasima 30000, Thailand

<sup>d</sup>State Key Laboratory of Advanced Technology for Materials Synthesis and Processing, Wuhan University of Technology, Wuhan 430070, China

<sup>e</sup>Research Unit of Adsorption, Catalysis & Energy Storage, Suranaree University of Technology, Nakhon Ratchasima 30000, Thailand

† Electronic supplementary information (ESI) available. See DOI: <https://doi.org/10.1039/d3ra06720c>


on hydrogen adsorption than surface chemistry.<sup>33</sup> Additionally, certain synthesized ACs demonstrated hydrogen uptake equivalent to those with lower surface area and pore volume.<sup>39–41</sup> These findings underline the need for a comprehensive understanding and further research in this field.

Due to the above reasons, it is challenging to investigate the individual characteristic properties of an adsorbent solely through experiments. Experimental observations are influenced by the interplay between various properties, making it challenging to control changes when synthesizing or modifying adsorbents to enhance specific properties. Experimental results indicate macroscopic behavior but cannot perfectly measure molecular-scale characteristics, mainly because of the combined effects of pore structure and surface functional group properties. To overcome these limitations, Grand Canonical Monte Carlo (GCMC) simulations have been employed. GCMC simulations offer macroscopic results that can be combined with experimental data, allowing for studying microscopic and molecular-scale phenomena. Using GCMC, it was reported that oxygen functional groups on graphene sheets significantly enhance hydrogen adsorption.<sup>42</sup> An optimum pore diameter of 0.68 nm was identified for hydrogen volumetric capacity at 25 °C and 25 bar.<sup>43</sup> Carbonaceous slit pore models were constructed with CO and COH groups grafted on surfaces in different pore sizes for H<sub>2</sub> storage at −196 °C,<sup>42</sup> in which the pore width was found to be the major factor for H<sub>2</sub> storage, greater than the heteroatom grafted on the solid surface. A pore width range was varied roughly in 0.7–1.5 nm of H<sub>2</sub> adsorption on a graphitic slit-pore at a range of −193 to 25 °C and pressure up to 200 bar,<sup>44</sup> with a pore width of 1.5 nm yielding the highest adsorption capacity. GCMC approaches have been employed to synthesize pore topologies such as slit-shape, nanotubes, and torusene for hydrogen storage.<sup>43,45</sup> Despite numerous experimental and simulated studies, the relationship between functional groups, pore width, and pore volume remains unclear across different pressure ranges. Additionally, understanding the molecular origin and heat contributions to overall hydrogen adsorption capacity in various carbonaceous materials is crucial. A comprehensive understanding of all aspects ranging from molecular origins to macroscopic behavior is essential for the sustainable large-scale application of hydrogen storage.

In this study, ACs were derived from jujube branches, an abundant and cost-effective agricultural waste found in Asian countries including Thailand. The synthesis of ACs involved physical heat treatment, KOH activation, and urea modification. These processes aimed to enhance nitrogen functional groups on the solid surface and improve the porous structure of the materials. The impact of activation temperature and duration and the characterization of physical and chemical properties were examined. Subsequently, the ACs were utilized for adsorbing hydrogen at the temperature range of −196 °C to 25 °C and pressure of up to 1 bar. Although pore width, volume, and surface chemistry have notable effects on adsorption, it is challenging to study them individually through experiments. To address this, a GCMC simulation was employed to systematically explore and gain insights into the molecular-level behavior of hydrogen adsorption.

## 2. Methods

### 2.1 Experimental

**2.1.1 Synthesis of O- and N-doped ACs.** Jujube (*Ziziphus mauritiana* Lam.) branches were cut and sieved into a particle size of 16 × 30 mesh and dried at 105 °C. Then, these were put into a horizontal ceramic tube furnace under an atmosphere of nitrogen with a flow rate of 100 ml min<sup>−1</sup> and a gradual increase in temperature with a heating rate of 5 °C min<sup>−1</sup> from room temperature to 600 °C which was held for 1 h. The sample was designated as biochar, as shown in Fig. 1.

For the activation stage, the biochar from the first step (carbonization) was placed in a horizontal ceramic tube furnace. The environment within the furnace was altered from an inert nitrogen atmosphere to a reactive carbon dioxide atmosphere to activate the biochar. Carbon dioxide was selected for its high oxidative capacity, which can enhance the yield of the process by preventing complete combustion of the carbon material. The biochar was heated from room temperature at a controlled rate of 5 °C min<sup>−1</sup> to the target temperatures of 800 °C or 900 °C and maintained at these temperatures for 1 hour. Following the completion of the heating cycle, the furnace was allowed to cool to room temperature under a nitrogen flow to preserve the activated carbon (AC) structure. The resulting AC was then collected and designated as AC<sub>x</sub>, where 'x' indicates the specific activation temperature utilized.

For pore and surface modification, a mixture of the biochar and urea (with a weight ratio of 1 : 1) was then oxidized with air at a flow rate of 100 ml min<sup>−1</sup> and heated at 350 °C with a heating rate of 5 °C min<sup>−1</sup> for 1 h. This was done to impregnate nitrogen functional groups grafted on the solid surface. Then, KOH solution was added to the sample with a weight ratio of 1 g sample per 2 g KOH. Afterward, this mixture was combined at room temperature using a magnetic stirrer for 24 h and then dried overnight in an oven at 120 °C. After that, the mixed sample was placed in a horizontal ceramic tube furnace under carbon dioxide at a flow rate of 100 ml min<sup>−1</sup>, with a gradual increase in temperature from room temperature to the desired temperature range (800–900 °C) at a heating rate of 5 °C min<sup>−1</sup>, and then held for the desired time (1 to 2 h). The sample was washed with hot water until the pH of the filtrate was neutral, and then it was dried at 105 °C for 24 h. The O and N co-doped AC was designated as N-AC<sub>x</sub>-y, where x and y refer to activation temperature and time, respectively.



Fig. 1 Synthesis of the original and modified ACs.



**2.1.2 Characterization.** The textural properties of the samples were analyzed using the nitrogen adsorption-desorption isotherm at  $-196\text{ }^{\circ}\text{C}$  using the BET Micromeritics (3 Flex). The sample was degassed for 6 h under vacuum at  $300\text{ }^{\circ}\text{C}$  before starting the measurement. The specific surface area ( $S_{\text{BET}}$ ) and pore size distribution were obtained from the multipoint Brunauer-Emmett-Teller (BET) equation and the non-local density functional theory (slit-pore model), respectively. The total pore volume ( $V_t$ ) was calculated by converting the amount of  $\text{N}_2$  adsorbed at a relative pressure of 0.95. The morphology and structure of samples were examined using scanning electron microscopy (SEM, JSM-6010LV) observations.

The surface chemistry was analyzed using Fourier-transform infrared spectroscopy (FTIR, Tensor 27) in the wave range of  $4000\text{--}400\text{ cm}^{-1}$  and X-ray photoelectron spectroscopy (XPS, Kratos Axis Ultra). In addition, the percentage of composition in the samples was characterized using the CHN elemental analyzer (LECO 628). Assuming that the amounts of other elements are negligible, the oxygen content is determined by the mass difference.

**2.1.3  $\text{H}_2$  adsorption measurements.** The  $\text{H}_2$  storage capacities were measured using the Micromeritics ASAP2020 plus instrument. ACs were evacuated to an ultrahigh vacuum at  $300\text{ }^{\circ}\text{C}$  for 12 h before starting the measurement.  $\text{H}_2$  sorption measurements were performed at different temperatures between  $-196$  and  $25\text{ }^{\circ}\text{C}$  over a pressure range of up to 1 bar.

The isosteric heat of  $\text{H}_2$  adsorption was calculated from isotherms at different temperatures between  $-196$  and  $25\text{ }^{\circ}\text{C}$  using the following Clausius-Clapeyron equation:

$$Q_{\text{st}} = -R \left[ \frac{\Delta(\ln P)}{\Delta\left(\frac{1}{T}\right)} \right]_n \quad (1)$$

where  $Q_{\text{st}}$  is the isosteric heat of adsorption at a specific loading ( $n$ ),  $T$  is the temperature,  $P$  is the pressure, and  $R$  is the ideal gas constant.

## 2.2 GCMC simulation

The isotherm and heat obtained from experimental works always originate from molecular origin derived from characteristic properties of adsorbents which are complex and could not be investigated separately on  $\text{H}_2$  adsorption behavior. Therefore, to overcome these limitations, GCMC simulations have been employed. To ensure and gain the accuracy of physical behavior each factor with a simple model was tuned independently from each other. The GCMC approach was carried out to study the effect of pore width, pore volume, surface functional group type, and concentration systematically. GCMC simulation details can be found in ref. 46 and 47. Fig. 2 presents two solid surface models used to explore surface chemistry. The adsorbent was modeled as an atomistic and graphitic slit pore with four graphene layers on each side of the solid walls. The simulation box's dimensions in the  $x$ ,  $y$ , and  $z$  directions were  $5.904\text{ nm}$ ,  $4.260\text{ nm}$ , and  $L_z$ , respectively, where  $L_z$  is the physical pore width. The functional group was grafted

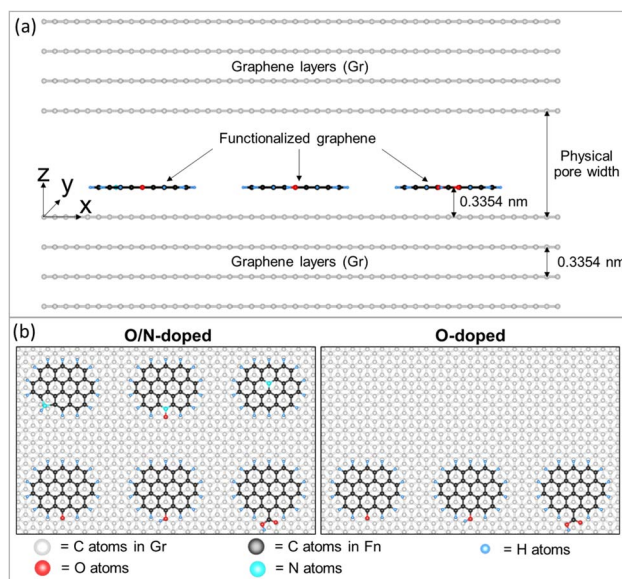


Fig. 2 (a) Side view ( $xz$  plane) of an atomistic solid model and (b) top view ( $xy$  plane) of the solid model representing functionalized graphene in different cases (O/N-doped AC and O-doped AC).

at the edge of a graphene sheet placed with its plate parallel to solid walls. In model 1, functionalized graphene with co-doped oxygen and nitrogen consisted of carbonyl (CO), hydroxyl (COH), carboxyl (COOH), pyrrolic (N5), pyridinic-N oxide (Ox-N6), and quaternary-N (NQ) groups. For model 2, graphene was functionalized with three oxygen groups (CO, COH, and COOH). The six functional groups in the model were selected because they are typically found in high intensity in ACs. Molecular parameters, including Lennard-Jones (LJ) 12-6 sites and partial charges of functional groups are summarized in Table S1 (ESI)<sup>†</sup> which have been collected from the literature.<sup>48–51</sup>

The interaction between  $\text{H}_2$  molecules and the graphite basal plane was calculated using the LJ 12-6 potential equation. The molecular parameters for the carbon atom in a graphene layer are obtained from Steele;<sup>52</sup> the intermolecular collision diameter ( $\sigma_i^{(s)}$ ) is  $0.34\text{ nm}$  and the depth of the potential well per Boltzmann constant ( $\epsilon_i^{(s)}/k_B$ ) is  $28\text{ K}$ . The distance between two graphene layers is  $0.3354\text{ nm}$ .

To describe the interaction between hydrogen molecules, the LJ 12-6 potential and the coulombic electrostatic equation were used in the calculation. The force field of the  $\text{H}_2$  molecule was taken from the literature.<sup>53</sup>  $\text{H}_2$  molecule was modeled as a single LJ 12-6 site at the center of the mass, with fixed charges at each H atom and center of mass along the H–H bond length of  $0.0741\text{ nm}$  to mimic the quadrupole moment of  $\text{H}_2$ . The molecular parameters are summarized in Table S1.<sup>†</sup>

The gravimetric  $\text{H}_2$  adsorption capacity ( $\rho_{\text{gra}}$ ) was calculated as the adsorbed amount divided by the sum of the masses of all atoms in the solid model ( $m_s$ ):

$$\rho_{\text{gra}} = \langle N \rangle / m_s \quad (2)$$





where  $\langle N \rangle$  is the average number of particles ( $H_2$  molecules) in the pore.

The total isosteric heat ( $q_{iso}$ ) is contributed from fluid–fluid (FF), fluid–functional group (FFn), and fluid–graphite basal plane (FGr) interactions together with kinetic energy ( $k_B T$ ) as shown in eqn (3):

$$q_{iso} = q_{FF} + q_{FFn} + q_{FGr} + k_B T \quad (3)$$

The isosteric heat from eqn (3) can be calculated from the fluctuation theory using the following equation:<sup>54</sup>

$$q_{A-B} = \frac{\langle U_{A-B} \rangle \langle N \rangle - \langle U_{A-B} N \rangle}{\langle N^2 \rangle - \langle N \rangle \langle N \rangle} \quad (4)$$

where  $U_{A-B}$  is the configuration energy of the system between entities A and B.

In this study, the alteration of density from the surface and the local density distribution of the center of each  $H_2$  site along the  $z$ -axis are calculated using eqn (5):

$$\rho(z) = \frac{\langle \Delta N_{z+\Delta z} \rangle}{L_x L_y \Delta z} \quad (5)$$

where  $L_x$  and  $L_y$  are the lengths of the slit-pore in the  $x$  and  $y$  directions, respectively, and  $\langle \Delta N_{z+\Delta z} \rangle$  is the average number of  $H_2$  site centers located in the confined areas  $z$  and  $z + \Delta z$ . During the sampling step in GCMC, the results of every 1000 configurations were collected to calculate the average values.

## 3. Results and discussion

### 3.1 Characterization

The  $N_2$  adsorption/desorption isotherms conducted at  $-196^\circ C$  for the synthesized samples exhibited type I behavior, as classified by the IUPAC classification (Fig. 3a). The significant rise in the isotherm at relatively low pressures ( $<0.1$ ) indicates not only characteristic micropore filling but also monolayer adsorption occurring in all pore sizes, including mesopores.<sup>55,56</sup> The  $N_2$  adsorbed amount in this pressure region was slightly higher for N-AC900 samples compared to AC900. The greater increase observed in N-AC900 samples can be attributed to the uptake of micropore filling and the monolayer on the mesopore surface, which is more abundant in N-AC900 samples. As shown in Fig. 3b, the ultra-micropore sizes ( $<0.7$  nm) were slightly reduced, while the supermicropore sizes (0.7–2.0 nm) and mesopores were developed and increased significantly. SEM images of all samples are presented in Fig. 4: the two hour modification shows a particularly clean surface with minimal pore blockage compared to the other ACs.

Table 1 presents the textural characteristics determined by  $N_2$  isotherms at  $-196^\circ C$  and the chemical characteristics obtained through elemental analysis for all ACs. The nitrogen content in the pristine ACs ranged 1.33–1.42% approximately by weight, depending on the precursor material. However, in modified ACs, the nitrogen groups were significantly enhanced, reaching 2.79–6.16% by weight. Additionally, the specific surface area and pore volume were developed and increased up to  $1118 \text{ m}^2 \text{ g}^{-1}$  and  $0.577 \text{ cm}^3 \text{ g}^{-1}$  respectively. Notably, the

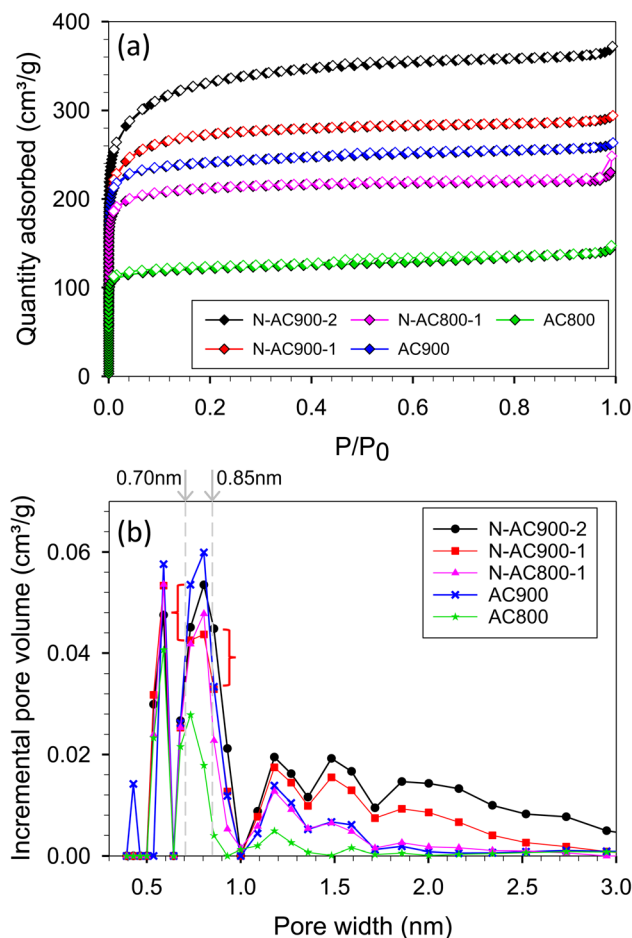


Fig. 3 (a)  $N_2$  adsorption/desorption isotherms at  $-196^\circ C$  and (b) pore size distributions.

modified ACs retained oxygen content alongside the increased nitrogen content. The N/O ratio of the modified ACs increased approximately 2–5 times compared to the original ACs.

The incorporation of KOH with  $CO_2$  during the activation process is a strategic step intended to enhance the development of a micro–mesoporous structure within the activated carbon matrix. KOH and  $CO_2$  act as a chemical activator, facilitating the widening of existing pores and the creation of new ones through a series of complex reactions that include dehydrogenation, aromatization, and cross-linking of carbon atoms. During nitrogen doping, where a potential concern is the blockage of pores and reduction in surface area due to the incorporation of nitrogenous groups, the use of KOH and  $CO_2$  can be particularly beneficial. It not only compensates for any potential loss of porosity but may also facilitate the doping process by creating more active sites for the nitrogen groups to attach. Thus, it can be concluded that the urea modification and KOH activation led to improvements in the microporous and mesoporous properties and nitrogen content in the N-doped ACs, as indicated by the increased  $S_{BET}$  and  $V_t$  with respect to the activation temperature and time.

To characterize the chemical properties of ACs, several measurements were used to support each other. Fig. 5 shows



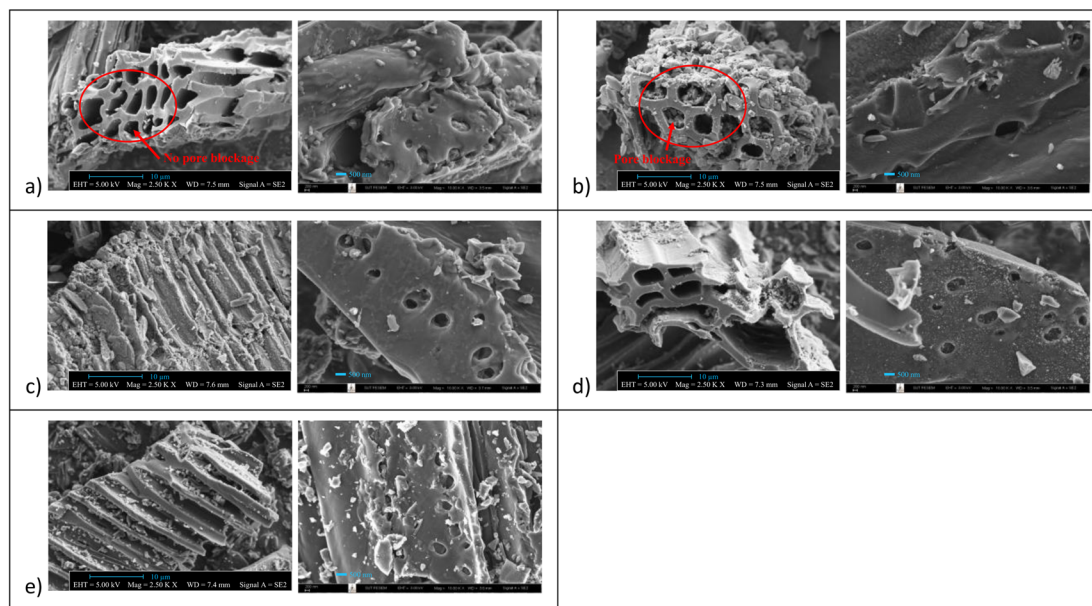


Fig. 4 SEM images of AC samples: (a) N-AC900-2, (b) N-AC900-1, (c) N-AC800-1, (d) AC900, and (e) AC800.

the FTIR results of ACs containing the functional groups. The bands at 3456, 2920, 1720, 1630, 1512, 1068, 879, and 472  $\text{cm}^{-1}$  can be identified as N-H/O-H, C-H, C=O, C=C, N-H, C-O, C-N, and C-C stretching respectively.<sup>57–60</sup> Additionally, O and N co-doped ACs displayed significant peaks of N-H, C-O, and C-N stretching, demonstrating the efficiency of

urea and KOH activation in enhancing the functional groups in AC.

Furthermore, the bonding configurations of N atoms were analyzed in detail through high-resolution N 1s XPS spectra (Fig. 6). The N 1s spectra were deconvoluted and assigned to specific N-containing groups, namely pyridinic-N or N6 (398.1

Table 1 Textural and chemical characteristics and  $\text{H}_2$  adsorption capacity at 1 bar of ACs

| ACs                | $S_{\text{BET}}$ ( $\text{m}^2 \text{g}^{-1}$ ) | $V_t$ ( $\text{cm}^3 \text{g}^{-1}$ ) | % components |      |       |       | $\text{H}_2$ uptake (wt%) |       | Year/ref.        |
|--------------------|---|---------------------------------------|--------------|------|-------|-------|---------------------------|-------|------------------|
|                    |   |                                       | C            | H    | N     | O     | −196 °C                   | 25 °C |                  |
| N-AC900-2          | 1118  | 0.577                                 | 83.30        | 0.02 | 2.79  | 13.88 | 2.62                      | 0.09  | The present work |
| N-AC900-1          | 918   | 0.456                                 | 83.40        | 0.01 | 5.34  | 11.25 | 2.59                      | 0.10  |                  |
| N-AC800-1          | 713   | 0.385                                 | 81.93        | 0.39 | 6.16  | 11.51 | 2.22                      | 0.11  |                  |
| AC900              | 812   | 0.409                                 | 83.81        | 0.66 | 1.42  | 14.10 | 2.28                      | 0.12  |                  |
| AC800              | 408   | 0.228                                 | 88.36        | 0.63 | 1.33  | 9.68  | 1.78                      | 0.11  |                  |
| NAC-800-3-1        | 2477.3  | 1.93                                  | 90.63        | 0.40 | 2.082 | 6.89  | 2.29                      |       | 2023 (ref. 11)   |
| LP_4               | 497.3   | 0.208                                 |              |      |       |       | 0.93                      |       | 2023 (ref. 12)   |
| Commercial AC      | 1678  | 0.73                                  | 90.8         |      | 0.6   | 8.6   | 1.98                      |       | 2023 (ref. 39)   |
| AC-He400-N500      | 1554  | 0.67                                  | 91.2         |      | 1.1   | 7.7   | 2.34                      |       |                  |
| NPC-1              | 2084.5  | 1.060                                 |              |      | 13.10 |       | 2.09                      |       | 2021 (ref. 40)   |
| NPC-2              | 3037.8  | 1.810                                 |              |      | 8.5   |       | 2.49                      |       |                  |
| NPC-3              | 3354.3  | 2.143                                 |              |      | 5.1   |       | 2.83                      |       |                  |
| NPC-4              | 3369.6  | 2.049                                 |              |      | 4.09  |       | 2.86                      |       |                  |
| AC500              | 809   | 0.34                                  |              |      |       |       | 1.45                      |       | 2020 (ref. 13)   |
| AC600              | 1251  | 0.53                                  |              |      |       |       | 1.89                      |       |                  |
| NAC                | 3263  | 1.75                                  |              |      | 1.64  |       | 2.91                      |       | 2019 (ref. 61)   |
| NAC3               | 3485  | 1.67                                  |              |      | 2.20  |       | 3.1                       |       | 2017 (ref. 62)   |
| PC-2-800           | 2919  | 1.425                                 |              |      | 0.98  |       | 2.71                      |       | 2016 (ref. 63)   |
| OB-CO <sub>2</sub> | 1185  | 0.52                                  | 90.2         | 0.48 | 0.48  | 6.25  | 1.69                      |       | 2016 (ref. 64)   |
| AC3                | 687.3   | 0.3624                                |              |      |       |       | 1.97                      |       | 2016 (ref. 65)   |
| C2-1/4-700         | 2370  | 1.08                                  | 92.2         | 0.6  |       | 7.1   | 2.50                      |       | 2011 (ref. 41)   |
| C4-1/2-700         | 1283  | 0.68                                  | 85.8         | 1.7  |       | 11.9  | 2.30                      |       |                  |
| Carbon C           | 1040  | 0.48                                  |              |      |       |       | 1.8                       |       | 2004 (ref. 66)   |
| JM1                | 890   | 0.65                                  |              |      |       |       | 1.2                       |       |                  |
| Norit R0,8         | 1320  | 0.65                                  |              |      |       |       | 1.6                       |       |                  |



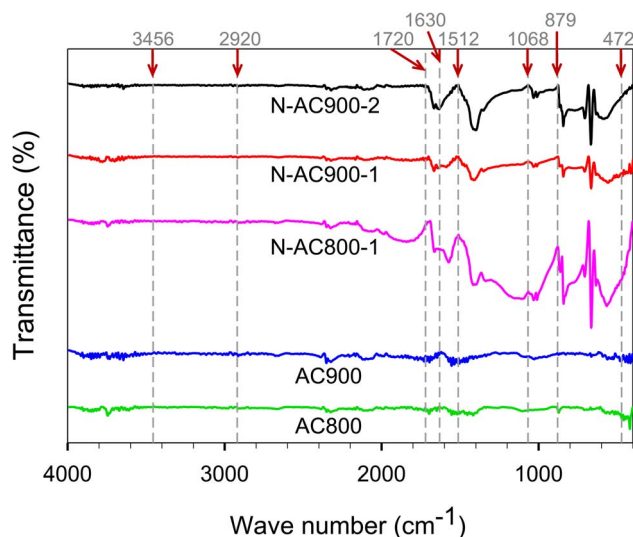


Fig. 5 FTIR spectra of AC samples.

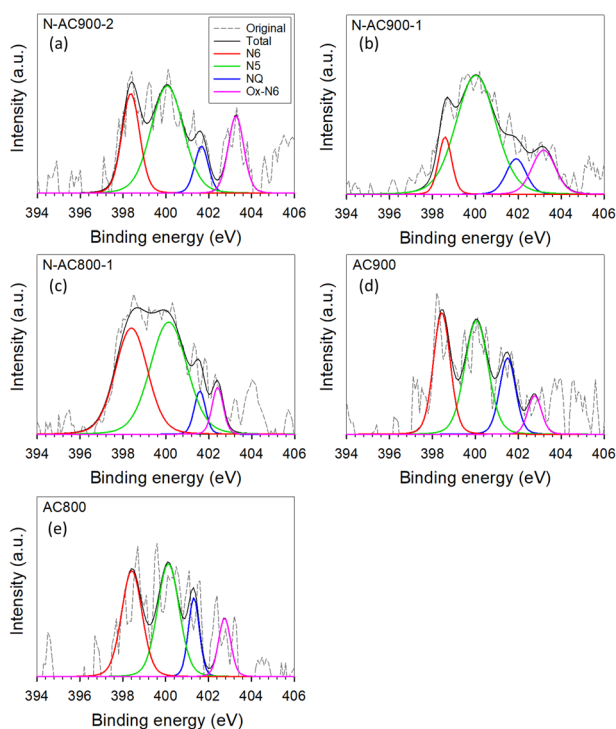


Fig. 6 XPS spectra of N 1s orbitals for all AC samples. (a) N-AC900-2, (b) N-AC900-1, (c) N-AC800-1, (d) AC900, and (e) AC800.

eV), pyrrolic-N or N5 (400.5 eV), quaternary-N or NQ (401.3 eV), and N-oxides or Ox-N6 (402–404 eV). It is evident that while all the AC samples derived from jujube branches exhibit similar N-containing species because of the inherent nature of the precursor, the relative abundance of these species within the samples varies significantly with activation temperature and time. N5 emerges as the dominant species across all samples, followed by N6, NQ, and Ox-N6. To provide a clearer visual representation, the ratios of each functional group in each

sample are presented in a bar chart (Fig. 7). Among these groups, NQ is the most stable, involving N atoms embedded in the graphene sheet with chemical bonds to the three neighboring carbon (C) atoms, which also makes it the most challenging group to form during synthesis, hence exhibiting the lowest content on the surface. N6 is the secondary group, while N5 and Ox-N6 are the tertiary groups. They are more likely to form at the edges or defects of the graphene sheet during surface modification. The presence of Ox-N6 was enhanced with a longer activation time or a higher temperature.

### 3.2 H<sub>2</sub> adsorption

To describe the isotherms, we divided the adsorption process into three regions based on the relative pressure ( $P/P_0$ ), as illustrated in the schematic diagram presented in Fig. 8.

**3.2.1 Region I: adsorption at low pressures.** The adsorbed amount in this region is dependent on the affinity of adsorbed phase where the strongest active site is for the adsorbate molecules to be adsorbed at low pressures or in the Henry law region. The affinity of an adsorbent is dependent on its physical and chemical properties including pore size, pore shape, and surface functional group properties, except for pore volume.

**3.2.2 Region II: adsorption at moderate pressures.** Once the strong active site was filled or covered by adsorbate molecules in region I, the rest of the adsorption phases in pores are then accommodated by the adsorbate in region II. The adsorbed amount in this region is influenced by the pore size or surface chemistry.

**3.2.3 Region III: adsorption at high pressures.** This region shows the packing of adsorbed molecules when the pore is full. The pore volume is the main factor in the packing amount. The secondary factor could be pore shape.

The H<sub>2</sub> adsorption isotherms at −196 and 25 °C are presented in Fig. 9, while the corresponding H<sub>2</sub> capacities at 1 bar are summarized in Table 1 and Fig. 10, allowing for comparison with values reported in the literature. The H<sub>2</sub> capacity obtained

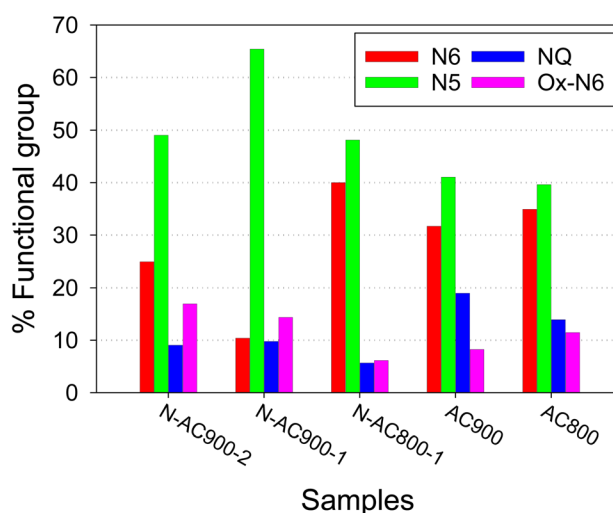


Fig. 7 Comparison of nitrogen functional group species on AC samples obtained from XPS.



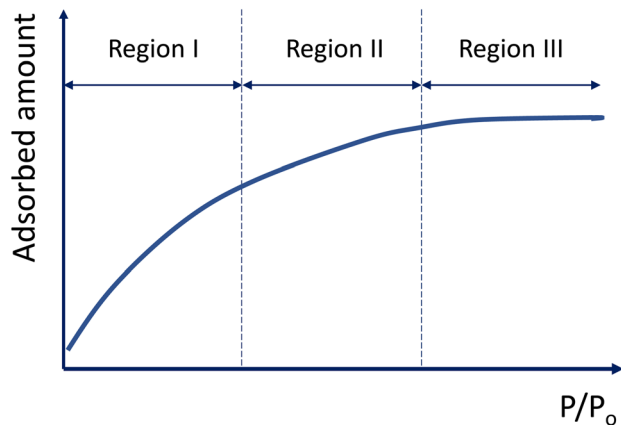


Fig. 8 Adsorption process with increasing relative pressure.

in this study at  $-196\text{ }^{\circ}\text{C}$  and 1 bar fell within the range of 1.78–2.62 wt%, which demonstrated promising potential as an alternative adsorbent. Interestingly, our modified ACs exhibited a specific surface area and pore volume approximately three times lower than other works; yet, their  $\text{H}_2$  capacities remained comparable. Furthermore, our modified ACs demonstrated higher  $\text{H}_2$  adsorption capacities compared to other ACs with similar surface areas or pore volumes. This can be attributed to the development of superior pore sizes in our modified ACs, which play a crucial role in achieving high capacity at this pressure range.

Analyzing the results at  $-196\text{ }^{\circ}\text{C}$  depicted in Fig. 9a, it was observed that the gravimetric capacity of the original ACs (AC900) surpassed that of the modified ACs (N-AC900-2) at low pressures ( $<0.25$  bar) during the adsorption process, specifically in region I. This happened despite AC900 having a lower pore volume and surface area. The reason behind this discrepancy lies in the strength of the strongest active site in AC900, which is stronger than that in the modified N-AC900-2. The dominant active site in AC900 is probably because of its pore size rather than its surface functional group. Notably, the main groups on the surface of AC900 are oxygen-containing, which are weaker compared to the abundant N groups found in N-AC900-2. The isosteric heat of AC900 correlates with the enhanced  $\text{H}_2$  capacity in this region.

Moving beyond the low loadings in region I, the modified ACs, particularly N-AC900-1 and N-AC900-2, exhibited enhanced  $\text{H}_2$  capacities compared to the other samples at higher pressures. In region II, the wider pore width played a key role in the gravimetric capacity. The adsorbed amount in N-AC900-2 surpassed that of AC900 because of the slightly greater development of superior pore sizes in N-AC900-2. This observation was a result of the interplay between pore size, pore volume, and surface chemistry, which can be further elucidated through a GCMC approach. It is important to note that none of the samples reached the adsorption capacity in region III, as the pressure was not sufficiently high to fully occupy the pores with adsorbate molecules.

Considering the interrelated loadings up to 0.12 wt% for isosteric heat calculations, which correspond to adsorption in

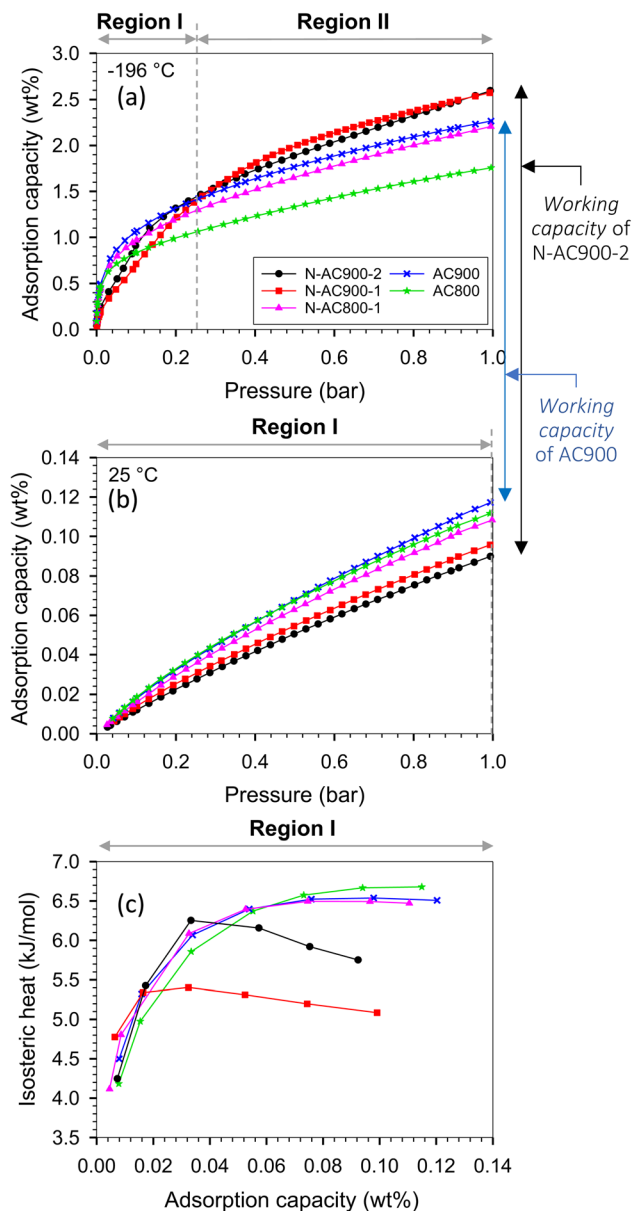


Fig. 9  $\text{H}_2$  adsorption isotherms at (a)  $-196$  and (b)  $25\text{ }^{\circ}\text{C}$  up to 1 bar, and (c) isosteric heat.

region I at both temperatures ( $-196$ ,  $25\text{ }^{\circ}\text{C}$ ), the isosteric heat represented only adsorption in region I, as depicted in Fig. 9c. Notably, N-AC900-1 and N-AC900-2 exhibited an additional advantage in terms of the released heat of adsorption, as their released heats were relatively lower compared to the other samples. This can be attributed to their larger pore sizes compared to the original ACs. The higher heat observed in AC900 was a result of interactions between the adsorbate and solid walls, including the opposite wall within smaller pore sizes.

At a temperature of  $25\text{ }^{\circ}\text{C}$ , adsorption up to 1 bar still occurred within region I (Fig. 9b), because of the higher value of saturated pressure ( $P_0$ ) at elevated temperature. Consequently, the adsorbed amounts in each adsorbent followed the same



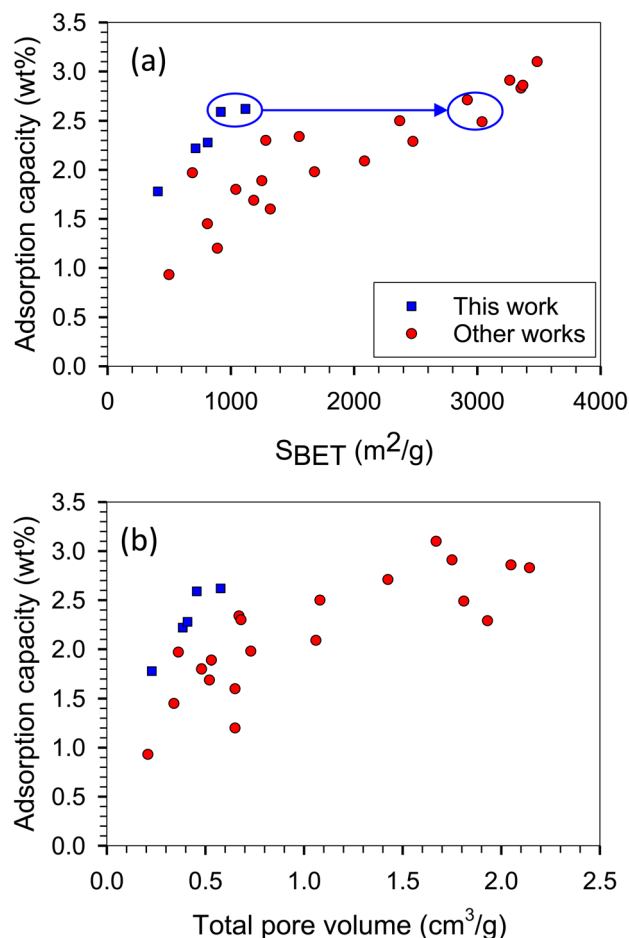


Fig. 10  $H_2$  adsorption capacity versus (a) specific surface area and (b) pore volume obtained with the present work and literature (other works) at  $-196^\circ\text{C}$  and 1 bar corresponding to Table 1.

order as in region I at  $-196^\circ\text{C}$ , with the capacity of the original ACs exceeding that of the modified ACs. From an application standpoint, an advantageous aspect is the ability to release  $H_2$  from the pores by increasing the temperature. Notably, the O and N co-doped ACs exhibited superior  $H_2$  storage capacities at  $-196^\circ\text{C}$  and, furthermore, facilitated a greater working capacity (useable capacity) of  $H_2$  from the pores at  $25^\circ\text{C}$  and 1 bar, surpassing the performance of the original ACs.

Regarding surface modification, simultaneous enhancements in functional group content and pore size, including pore volume, were achieved. However, a comprehensive and systematic investigation of each property is necessary, which is challenging to conduct solely through experimental approaches. In order to provide further support and deepen the understanding of our experimental observations, it is essential to systematically explore the relationship between  $H_2$  adsorption capacity and key properties such as pore width, pore volume, and functional group type. This can be accomplished through the application of GCMC simulations. By employing such simulations, we can gain valuable insights into the underlying mechanisms governing  $H_2$  adsorption behavior in our modified ACs.

### 3.3 Effect of pore size, pore volume, and surface chemistry obtained with GCMC

Firstly, we validated our simulations obtained with our in-house-program code for  $H_2$  adsorption on graphite surface at  $-195.80$  and  $-196.15^\circ\text{C}$  obtained from experimental data.<sup>67,68</sup> The graphite surface was modeled as an atomistic model with four graphene layers, which are enough number to form as a graphite (Fig. 11). We found that the simulated results agreed very well with experimental data for all studied temperatures. Therefore, our program code merits to be used for other cases such as adsorption in graphitic pores.

In the case of adsorption in pores, the specific surface area of adsorbent models is constant while the pore volume increases with increasing pore width. The gravimetric capacity at various pressures and pore widths is presented in Fig. 12a and b. There were three features on the plot depending on pressure ranges at  $-196^\circ\text{C}$  (Fig. 12a). The first feature was at low pressures ( $<0.3$  bar), where the optimum pore width was found at 0.65 nm, at which point the single monolayer was complete by adsorbate (see the local density distributions and snapshots in Fig. S1†). The second feature was found in the moderate pressure range (0.3–15 bar), where the highest capacity was found at pore widths of 0.95–1.5 nm depending on pressure. Therefore, for the first time, the optimum pore widths were plotted as a function of pressure as shown in Fig. 12c. The optimum pore width of 0.95 nm fitted a completely double monolayer, while the pore widths of 1.20–1.25 nm fitted a three-layer formation (Fig. S1†). Indeed, the superior pore sizes showed a range of 0.8–1.3 nm at a pressure of 1 bar (Fig. 12a). It should be noted that this pore-size range (0.8–1.3 nm) was enhanced in the modified ACs, especially N-AC900-1 and N-AC900-2, to achieve superior uptake at 1 bar. Noticeably, during these pressure ranges (low and moderate pressures), the larger pore volume did not give the greater  $H_2$  adsorption capacity. However, at higher pressures ( $>15$  bar), the third feature indicated that pore volume plays a greater role in capacity rather than pore width. It should be noted in this case that the larger pore width had a higher

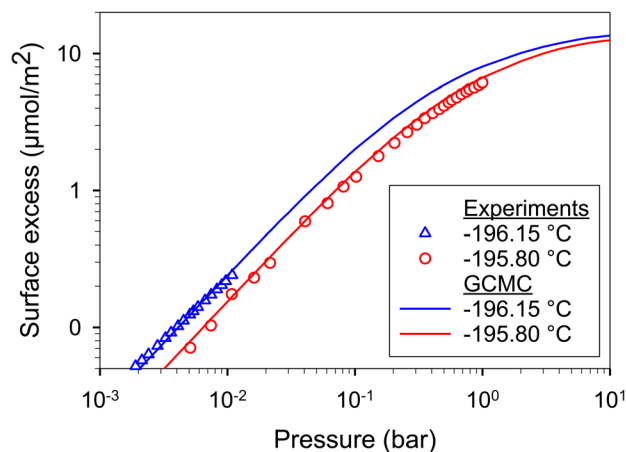


Fig. 11  $H_2$  adsorption on graphite surface at  $-196.15$  and  $-195.80^\circ\text{C}$  obtained with GCMC (this work) and experimental data.<sup>67,68</sup>





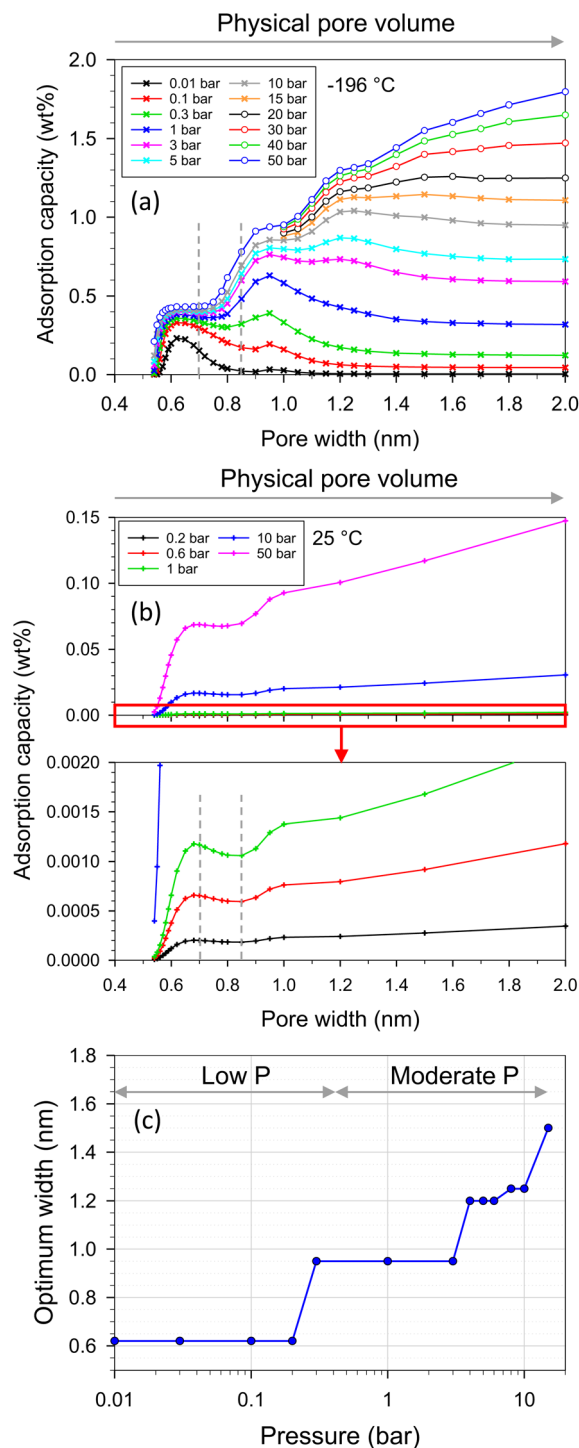


Fig. 12  $\text{H}_2$  adsorption capacity versus pore width and pore volume at (a)  $-196$  and (b)  $25$  °C, (c) optimum width versus pressure at  $-196$  °C obtained with GCMC.

gravimetric capacity than the smaller pore width because of the increased pore volume for enhanced packing.

On the other hand, when temperature increased to  $25$  °C, the behavior on the plot (Fig. 12b) exhibited two features depending on the pore width ranges for all studied pressures (up to 50 bar): (i) during the pore width range up to  $0.85$  nm, the optimum

width was found to be  $0.68$  nm, which was fit for a completely single monolayer. This optimum width was slightly larger than that of  $-196$  °C because of the high energy of fluid motion at  $25$  °C. (ii) At a pore width larger than  $0.85$  nm, the  $\text{H}_2$  capacity increased with pore volume.

We put all the functional group types on the bottom wall to investigate the competition between each functional group type in the same pore. The adjacent groups were far enough from each other to be isolated, avoiding the dependent configuration between them. It should be noted that the adsorbate–adsorbent interaction directly influences the adsorbed amount in the pore. Adsorbate molecules began to adsorb at the strongest active site until it became saturated or completely covered by adsorbate molecules. The additional adsorbate molecules were then adsorbed on the less active site. The active sites could be either of optimum pore size or, having a surface functional group, or having a combination of these two properties. However, temperature is one of the main factors that plays an important role in adsorbed amount. The feature that was found between the original ACs versus the modified ACs in Fig. 9 could be described using the results plotted in Fig. 13. This resulted from the interplays between the characteristic properties of each adsorbent. For example, the pore size and pore volume of the modified N-AC900-2 (O/N doped) were greater than those of the original AC900 (O-doped). In Fig. 13, there were two solid models, including O-doped AC and O/N-doped AC. These two adsorbent models had different surface functional groups, pore sizes, and pore volumes. We modeled the O/N-doped AC with a larger pore width ( $0.85$  nm) and larger pore volume to represent the modified ACs (e.g., N-AC900-2) compared to those values of the original ACs (e.g., AC900). The O-doped AC model representing AC900 had a smaller pore width ( $0.70$  nm) and a smaller pore volume. Possibly, these pore widths were selected based on the pore size developed by the modification, as shown in Fig. 3b. The results showed that the  $\text{H}_2$  capacity at  $-196$  °C obtained with O-doped AC was more concave and higher than that of O/N-doped AC at low pressures (region I). Because the pore size of the O-doped AC was dominated at low pressures rather than the pore size of the O/N-doped AC, the pore size of the O-doped AC was more effective and was stronger as an active site than its surface functional group, as confirmed by the heat contributions in Fig. 13. Similarly, during the adsorption at the pressure range, up to 1 bar was still the adsorption in region I at higher temperature of  $25$  °C, whereas the adsorption at  $-196$  °C could proceed up to region II, where the  $\text{H}_2$  capacity in O/N-doped AC became higher than the O-doped AC. The O/N-doped AC with a pore width of  $0.85$  nm was superior and able to be accommodated with two-layer formation, whereas the smaller pore width of the O-doped AC could fit only a single monolayer, as shown by the local density distributions and snapshots in Fig. 14 and S2.† In region II, the isotherm at  $-196$  °C of O-doped AC showed a plateau, indicating that the pore filling was almost complete. Therefore, our simulated results revealed the molecular origin of the macroscopic behavior, which is consistent with the observation in the experimental data (Fig. 9).



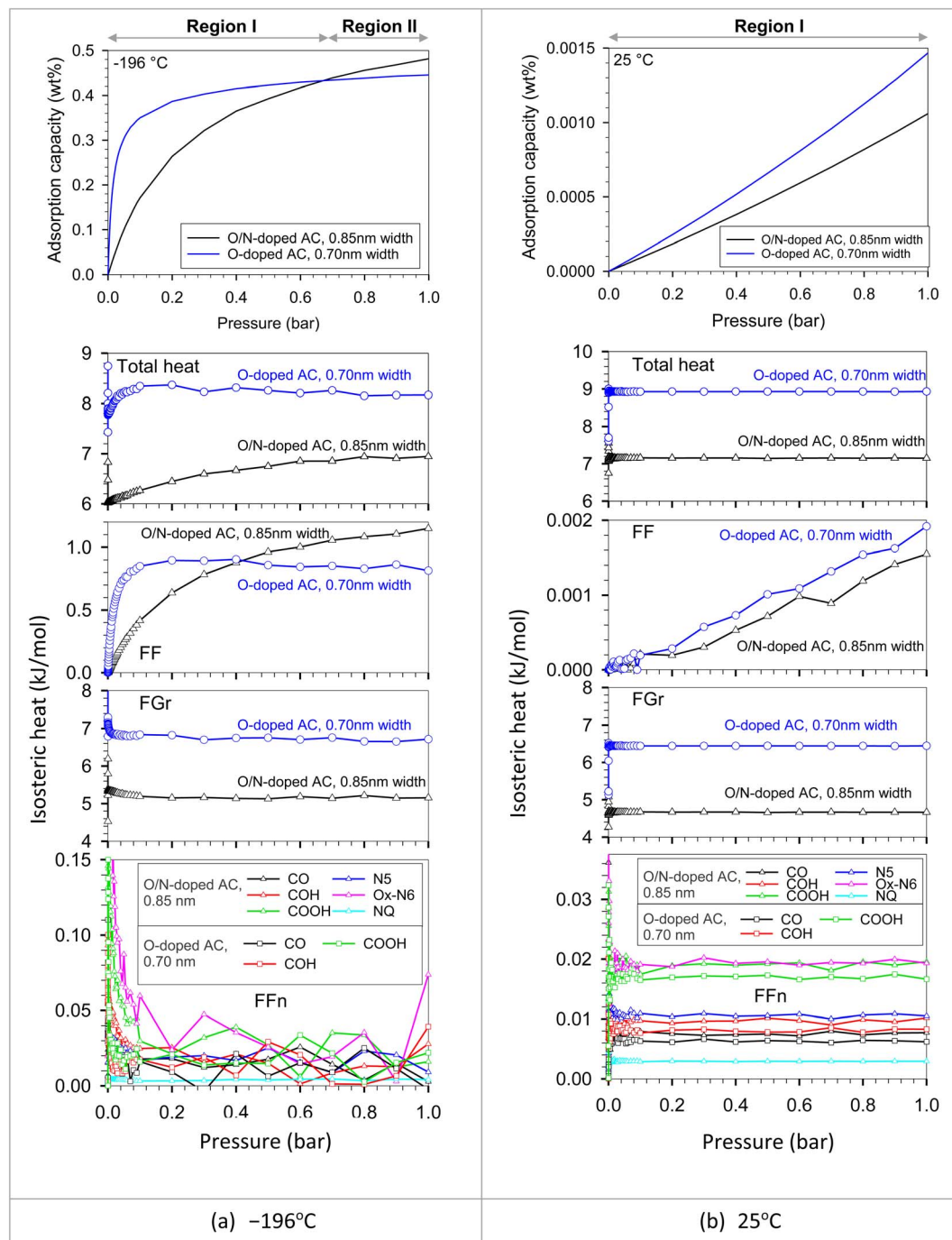


Fig. 13 Isotherms and isosteric heats of  $H_2$  adsorption in O/N-doped AC model (0.85 nm width) and O-doped AC model (0.70 nm width) at (a)  $-196$  and (b)  $25^\circ\text{C}$  obtained with GCMC.

In addition, the heat contributions indicated particularly that Ox-N6 and COOH are about two times stronger than other groups. Among O groups, COOH has the strongest interaction with  $H_2$  because its number of sites is higher than that of other O groups. As a result, the potential can be classified in the order of Ox-N6 > COOH > N5 > COH > CO > NQ. To illustrate the effect of surface chemistry and to ignore the effect of pore width on the  $H_2$  adsorption capacity in different pressure ranges, the different functionalized surface models (O/N-doped *versus* O-

doped) with the same pore width were simulated and compared as shown in Fig. S3.† The simulated results showed that the surface chemistry can control the  $H_2$  uptake only at low and moderate pressure ranges. Accordingly,  $H_2$  molecules were adsorbed in the functional groups at low pressures because of the strong FFn interactions until they become saturated by adsorbate molecules at a pressure of about 1.5 bar (these cases), where the FFn heat dramatically decreased to zero. When pressure was further increased, the adsorption behavior in



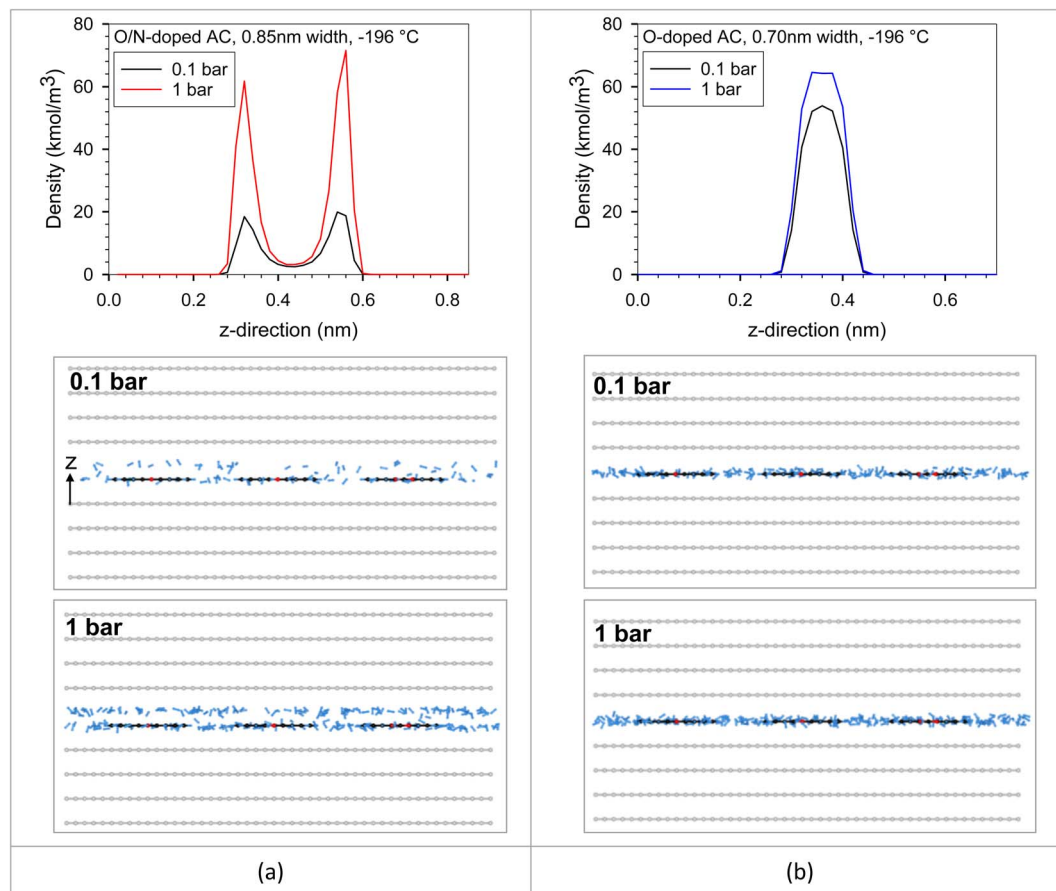


Fig. 14 Local density distributions in z-direction and snapshots of  $\text{H}_2$  adsorption in (a) O/N-doped AC model (0.85 nm width) and (b) O-doped AC model (0.70 nm width) at  $-196^\circ\text{C}$ .

these two solid models reached the same levels, followed by the same manner. However, according to the adsorbed amount changed with individual factors, pore size was the most factor while surface chemistry was the second factor during the effective pressures (up to 1.5 bar).

## 4. Conclusions

O and N co-doped AC were successfully synthesized by utilizing jujube branches, an agricultural waste, through a combination of heat and chemical treatments. In the synthesis process, urea was impregnated into the original AC as a nitrogen source, followed by activation using KOH heat treatment to transform it into an O and N co-doped AC. This modification not only enhanced the presence of N groups, but also resulted in the development and increase of superior pore sizes (0.8–1.3 nm), specific surface area, and pore volume. The modified AC, referred to as O and N co-doped AC, exhibited a remarkable enhancement in  $\text{H}_2$  adsorption capacity, reaching up to 2.62 wt% at  $-196^\circ\text{C}$  and 1 bar, surpassing the performance of several other ACs reported in the literature. In terms of application, the presence of superior pore sizes not only contributed to an increased  $\text{H}_2$  adsorption capacity, but also resulted in lower heat of adsorption, making it advantageous for cooling

applications. Moreover, the modified O and N co-doped AC demonstrated a higher  $\text{H}_2$  storage capacity at  $-196^\circ\text{C}$  and a greater release of  $\text{H}_2$  from the pores at  $25^\circ\text{C}$  and 1 bar compared to the original AC.

To further investigate and support our experimental observations, we employed a GCMC approach. This allowed us to explore the influence of functional group type, pore width, and pore volume on the observed  $\text{H}_2$  adsorption behavior. Our GCMC simulations provided detailed insights into the heat contributions and molecular origin, thereby improving our understanding of the isotherms. At low pressures ( $<0.3$  bar), an optimum pore width of 6.5 nm was identified, facilitating the completion of a single monolayer of adsorbate. In the moderate pressure range (0.3–15 bar), the highest capacity was observed at a pore width range of 0.95–1.5 nm depending on pressure. Notably, the modified AC with superior pore sizes in the range of 0.8–1.3 nm exhibited enhanced uptake at 1 bar. However, at higher pressures ( $>15$  bar), the pore volume played a more significant role in determining the capacity rather than the pore width. Surface chemistry played a crucial role in  $\text{H}_2$  uptake at low and moderate pressures until saturation was reached by adsorbate molecules. The  $\text{H}_2$ -functional group interaction followed the order of  $\text{Ox-N6} > \text{COOH} > \text{N5} > \text{COH} > \text{CO} > \text{NQ}$  within the same pore. Not only the superior pore sizes but also the Ox-

N6 was likely enhanced on solid surface during the modification with temperature and time in our experimental works. Our simulated results demonstrated good agreement with experimental data and offered a potential strategy for enhancing pore size and surface chemistry to achieve superior H<sub>2</sub> storage in porous carbons across a wide pressure range, including low, moderate, and high pressures.

## Author contributions

Suphakorn Anuchitsakol: investigation, methodology, formal analysis, writing – original draft, visualization. Waralee Dilokkunakul: methodology, formal analysis, writing – original draft, visualization. Numphueng Khongtor: formal analysis, writing – review & editing, software, visualization. Somboon Chaemchuen: visualization, writing – review & editing. Nikom Klomkliang: investigation, methodology, formal analysis, resources, software, validation, writing – review & editing, supervision.

## Conflicts of interest

There are no conflicts to declare.

## Acknowledgements

This work was supported by Suranaree University of Technology (SUT) and by Thailand Science Research and Innovation (TSRI) (Full-time61/05/2565). The authors acknowledge National e-Science Infrastructure Consortium for providing computing resources that have contributed to the research results reported within this paper.

## References

- BP, *bp Energy Outlook 2023 edition*, <https://www.bp.com/content/dam/bp/business-sites/en/global/corporate/pdfs/energy-economics/energy-outlook/bp-energy-outlook-2023.pdf>, accessed Jun 20, 2023.
- C. D. Thomas, A. Cameron, R. E. Green, M. Bakkenes, L. J. Beaumont, Y. C. Collingham, B. F. N. Erasmus, M. F. de Siqueira, A. Grainger, L. Hannah, L. Hughes, B. Huntley, A. S. van Jaarsveld, G. F. Midgley, L. Miles, M. A. Ortega-Huerta, A. Townsend Peterson, O. L. Phillips and S. E. Williams, Extinction risk from climate change, *Nature*, 2004, **427**, 145–148.
- G.-R. Walther, E. Post, P. Convey, A. Menzel, C. Parmesan, T. J. C. Beebee, J.-M. Fromentin, O. Hoegh-Guldberg and F. Bairlein, Ecological responses to recent climate change, *Nature*, 2002, **416**, 389–395.
- G. Nazir, A. Rehman, S. Hussain, S. Aftab, K. Heo, D. M. Ikram, D. S. Patil and M. A. Ud Din, Recent advances and reliable assessment of solid-state materials for hydrogen storage: a step forward toward a sustainable H<sub>2</sub> economy, *Adv. Sustainable Syst.*, 2022, **6**, 2200276.
- O. Czakkel, B. Nagy, G. Dobos, P. Fouquet, E. Bahn and K. László, Static and dynamic studies of hydrogen adsorption on nanoporous carbon gels, *Int. J. Hydrogen Energy*, 2019, **44**, 18169–18178.
- Y. Xia, Z. Yang and Y. Zhu, Porous carbon-based materials for hydrogen storage: advancement and challenges, *J. Mater. Chem. A*, 2013, **1**, 9365–9381.
- Y.-J. Heo and S.-J. Park, Synthesis of activated carbon derived from rice husks for improving hydrogen storage capacity, *J. Ind. Eng. Chem.*, 2015, **31**, 330–334.
- I. Wróbel-Iwaniec, N. Diez and G. Gryglewicz, Chitosan-based highly activated carbons for hydrogen storage, *Int. J. Hydrogen Energy*, 2015, **40**, 5788–5796.
- T. Kopac, Y. Kirca and A. Toprak, Synthesis and characterization of KOH/boron modified activated carbons from coal and their hydrogen sorption characteristics, *Int. J. Hydrogen Energy*, 2017, **42**, 23606–23616.
- C.-C. Huang, H.-M. Chen and C.-H. Chen, Hydrogen adsorption on modified activated carbon, *Int. J. Hydrogen Energy*, 2010, **35**, 2777–2780.
- H. Zhang, Y. Zheng and Y. Cui, Melamine assisted preparation of nitrogen doped activated carbon from sustainable biomass for H<sub>2</sub> and CO<sub>2</sub> storage, *Int. J. Hydrogen Energy*, 2023, **48**, 17914–17922.
- E. De Rose, S. Bartucci, C. P. Bonaventura, G. Conte, R. G. Agostino and A. Policicchio, Effects of activation temperature and time on porosity features of activated carbons derived from lemon peel and preliminary hydrogen adsorption tests, *Colloids Surf., A*, 2023, **672**, 131727.
- A. Toprak, Production and characterization of microporous activated carbon from cherry laurel (*Prunus laurocerasus* L.) stone: application of H<sub>2</sub> and CH<sub>4</sub> adsorption, *Biomass Convers. Biorefin.*, 2020, **10**, 977–986.
- G. Nazir, A. Rehman, S. Hussain, A. M. Afzal, G. Dastgeer, M. A. Rehman, Z. Akhter, T. I. Al-Muhimeed and A. A. AlObaid, Heteroatoms-doped hierarchical porous carbons: multifunctional materials for effective methylene blue removal and cryogenic hydrogen storage, *Colloids Surf., A*, 2021, **630**, 127554.
- H. W. Langmi, J. Ren, B. North, M. Mathe and D. Bessarabov, Hydrogen storage in metal-organic frameworks: a review, *Electrochim. Acta*, 2014, **128**, 368–392.
- N. M. Musyoka, J. Ren, H. W. Langmi, B. C. North, M. Mathe and D. Bessarabov, Synthesis of rGO/Zr-MOF composite for hydrogen storage application, *J. Alloys Compd.*, 2017, **724**, 450–455.
- S.-Y. Lee and S.-J. Park, Effect of platinum doping of activated carbon on hydrogen storage behaviors of metal-organic frameworks-5, *Int. J. Hydrogen Energy*, 2011, **36**, 8381–8387.
- Z. W. Zhu and Q. R. Zheng, Investigation of cryo-adsorption hydrogen storage capacity of rapidly synthesized MOF-5 by mechanochemical method, *Int. J. Hydrogen Energy*, 2023, **48**, 5166–5174.
- K. S. Deeg, J. J. Gutiérrez-Sevillano, R. Bueno-Pérez, J. B. Parra, C. O. Ania, M. Doblaré and S. Calero, Insights on the molecular mechanisms of hydrogen adsorption in zeolites, *J. Phys. Chem. C*, 2013, **117**, 14374–14380.





- 20 Z. Yang, Q. Jia, B. Chen, X. Gou, Y. Zhu and Y. Xia, Hydrogen adsorption properties of in situ synthesized Pt-decorated porous carbons templated from zeolite EMC-2, *Int. J. Hydrogen Energy*, 2020, **45**, 25086–25095.
- 21 S. Kumar, R. Bera, N. Das and J. Koh, Chitosan-based zeolite-Y and ZSM-5 porous biocomposites for H<sub>2</sub> and CO<sub>2</sub> storage, *Carbohydr. Polym.*, 2020, **232**, 115808.
- 22 X. Wang, H. Cheng, G. Ye, J. Fan, F. Yao, Y. Wang, Y. Jiao, W. Zhu, H. Huang and D. Ye, Key factors and primary modification methods of activated carbon and their application in adsorption of carbon-based gases: a review, *Chemosphere*, 2022, **287**, 131995.
- 23 M. Mohan, V. K. Sharma, E. A. Kumar and V. Gayathri, Hydrogen storage in carbon materials—a review, *Energy Storage*, 2019, **1**, e35.
- 24 Y. Maneewong, S. Chaemchuen, F. Verpoort and N. Klomkliang, Paracetamol removal from water using N-doped activated carbon derived from coconut shell: kinetics, equilibrium, cost analysis, heat contributions, and molecular-level insight, *Chem. Eng. Res. Des.*, 2022, **185**, 163–175.
- 25 K. Mainali, S. H. Mood, M. R. Pelaez-Samaniego, V. Sierra-Jimenez and M. Garcia-Perez, Production and applications of N-doped carbons from bioresources: a review, *Catal. Today*, 2023, **423**, 114248.
- 26 D. R. Lobato-Peralta, E. Duque-Brito, A. Ayala-Cortés, D. M. Arias, A. Longoria, A. K. Cuentas-Gallegos, P. J. Sebastian and P. U. Okoye, Advances in activated carbon modification, surface heteroatom configuration, reactor strategies, and regeneration methods for enhanced wastewater treatment, *J. Environ. Chem. Eng.*, 2021, **9**, 105626.
- 27 D. Saha and M. J. Kienbaum, Role of oxygen, nitrogen and sulfur functionalities on the surface of nanoporous carbons in CO<sub>2</sub> adsorption: a critical review, *Microporous Mesoporous Mater.*, 2019, **287**, 29–55.
- 28 T. K. Das, S. Banerjee, P. Sharma, V. Sudarsan and P. U. Sastry, Nitrogen doped porous carbon derived from EDTA: effect of pores on hydrogen storage properties, *Int. J. Hydrogen Energy*, 2018, **43**, 8385–8394.
- 29 J. Huang, Y. Liang, H. Dong, H. Hu, P. Yu, L. Peng, M. Zheng, Y. Xiao and Y. Liu, Revealing contribution of pore size to high hydrogen storage capacity, *Int. J. Hydrogen Energy*, 2018, **43**, 18077–18082.
- 30 E. Masika and R. Mokaya, Hydrogen storage in high surface area carbons with identical surface areas but different pore sizes: direct demonstration of the effects of pore size, *J. Phys. Chem. C*, 2012, **116**, 25734–25740.
- 31 M. Sevilla, R. Mokaya and A. B. Fuertes, Ultrahigh surface area polypyrrole-based carbons with superior performance for hydrogen storage, *Energy Environ. Sci.*, 2011, **4**, 2930–2936.
- 32 A. Rehman, G. Nazir, K. Heo, S. Hussain, M. Ikram, Q. Mahmood, T. Alshahrani and H. S. M. Abd-Rabbob, Single step strategy to prepare highly microporous carbons derived from melamine and terephthalaldehyde for high-performance material-based hydrogen storage, *J. Energy Storage*, 2023, **66**, 107468.
- 33 Y. Gogotsi, C. Portet, S. Osswald, J. M. Simmons, T. Yildirim, G. Laudisio and J. E. Fischer, Importance of pore size in high-pressure hydrogen storage by porous carbons, *Int. J. Hydrogen Energy*, 2009, **34**, 6314–6319.
- 34 C. Zhang, Z. Geng, M. Cai, J. Zhang, X. Liu, H. Xin and J. Ma, Microstructure regulation of super activated carbon from biomass source corncob with enhanced hydrogen uptake, *Int. J. Hydrogen Energy*, 2013, **38**, 9243–9250.
- 35 W. Zhao, V. Fierro, N. Fernández-Huerta, M. T. Izquierdo and A. Celzard, Hydrogen uptake of high surface area-activated carbons doped with nitrogen, *Int. J. Hydrogen Energy*, 2013, **38**, 10453–10460.
- 36 M. Sevilla, A. B. Fuertes and R. Mokaya, Preparation and hydrogen storage capacity of highly porous activated carbon materials derived from polythiophene, *Int. J. Hydrogen Energy*, 2011, **36**, 15658–15663.
- 37 M. Sevilla, R. Foulston and R. Mokaya, Superactivated carbide-derived carbons with high hydrogen storage capacity, *Energy Environ. Sci.*, 2010, **3**, 223–227.
- 38 L. S. Blankenship, N. Balahmar and R. Mokaya, Oxygen-rich microporous carbons with exceptional hydrogen storage capacity, *Nat. Commun.*, 2017, **8**, 1545.
- 39 A. Morandé, P. Lillo, E. Blanco, C. Pazo, A. B. Dongil, X. Zarate, M. Saavedra-Torres, E. Schott, R. Canales, A. Videla and N. Escalona, Modification of a commercial activated carbon with nitrogen and boron: hydrogen storage application, *J. Energy Storage*, 2023, **64**, 107193.
- 40 R. Mishra, P. R. Prasad, P. Panda and S. Barman, Highly porous activated N-doped carbon as an ideal electrode material for capacitive energy storage and physisorption of H<sub>2</sub>, CO<sub>2</sub>, and CH<sub>4</sub>, *Energy Fuels*, 2021, **35**, 14177–14187.
- 41 M. Sevilla, A. B. Fuertes and R. Mokaya, High density hydrogen storage in superactivated carbons from hydrothermally carbonized renewable organic materials, *Energy Environ. Sci.*, 2011, **4**, 1400–1410.
- 42 A. Gotzias, E. Tylianakis, G. Froudakis and T. Steriotis, Theoretical study of hydrogen adsorption in oxygen functionalized carbon slit pores, *Microporous Mesoporous Mater.*, 2012, **154**, 38–44.
- 43 D. Caviedes and I. Cabria, Grand canonical Monte Carlo simulations of the hydrogen storage capacities of slit-shaped pores, nanotubes and torusenes, *Int. J. Hydrogen Energy*, 2022, **47**, 11916–11928.
- 44 S. Karki and S. N. Chakraborty, A Monte Carlo simulation study of hydrogen adsorption in slit-shaped pores, *Microporous Mesoporous Mater.*, 2021, **317**, 110970.
- 45 S. Karki and S. N. Chakraborty, Hydrogen adsorption in nanotube and cylindrical pore: a grand canonical Monte Carlo simulation study, *Int. J. Hydrogen Energy*, 2023, **48**, 2731–2741.
- 46 N. Klomkliang, N. Khongtor, P. Phadungbut, S. Chaemchuen and D. Nicholson, Atomic heat contributions for carbon dioxide adsorption in IRMOF-1, *Ind. Eng. Chem. Res.*, 2021, **60**, 12650–12662.



- 47 P. Teerachawanwong, W. Dilokekunakul, P. Phadungbut, N. Klomkliang, S. Supasitmongkol, S. Chaemchuen and F. Verpoort, Insights into the heat contributions and mechanism of CO<sub>2</sub> adsorption on metal-organic framework MIL-100 (Cr, Fe): experiments and molecular simulations, *Fuel*, 2023, **331**, 125863.
- 48 M. Jorge, C. Schumacher and N. A. Seaton, Simulation study of the effect of the chemical heterogeneity of activated carbon on water adsorption, *Langmuir*, 2002, **18**, 9296–9306.
- 49 P. Psarras, J. He and J. Wilcox, Effect of water on the CO<sub>2</sub> adsorption capacity of amine-functionalized carbon sorbents, *Ind. Eng. Chem. Res.*, 2017, **56**, 6317–6325.
- 50 C. M. Tenney and C. M. Lastoskie, Molecular simulation of carbon dioxide adsorption in chemically and structurally heterogeneous porous carbons, *Environ. Prog.*, 2006, **25**, 343–354.
- 51 K. P. Travis and K. E. Gubbins, Transport diffusion of oxygen–nitrogen mixtures in graphite pores: a nonequilibrium molecular dynamics (NEMD) study, *Langmuir*, 1999, **15**, 6050–6059.
- 52 W. A. Steele, The physical interaction of gases with crystalline solids: I. Gas-solid energies and properties of isolated adsorbed atoms, *Surf. Sci.*, 1973, **36**, 317–352.
- 53 E. Pantatosaki and G. K. Papadopoulos, On the computation of long-range interactions in fluids under confinement: application to pore systems with various types of spatial periodicity, *J. Chem. Phys.*, 2007, **127**, 164723.
- 54 D. Nicholson and N. G. Parsonage, *Computer Simulation and the Statistical Mechanics of Adsorption*, Academic Press, London, 1982.
- 55 N. Klomkliang, D. D. Do and D. Nicholson, Effects of temperature, pore dimensions and adsorbate on the transition from pore blocking to cavitation in an ink-bottle pore, *Chem. Eng. J.*, 2014, **239**, 274–283.
- 56 N. Klomkliang, D. D. Do and D. Nicholson, Hysteresis loop and scanning curves for argon adsorbed in mesopore arrays composed of two cavities and three necks, *J. Phys. Chem. C*, 2015, **119**, 9355–9363.
- 57 M. Aho, P. Kortelainen, J. Rantanen and V. Linna, Pyrolysis of peat studied by thermogravimetry and Fourier transform infrared spectroscopy, *J. Anal. Appl. Pyrolysis*, 1989, **15**, 297–306.
- 58 J. Simitzis and J. Sfyraakis, Pyrolysis of lignin biomass—novolac resin for the production of polymeric carbon adsorbents, *J. Anal. Appl. Pyrolysis*, 1993, **26**, 37–52.
- 59 Q. Li, J. Yang, D. Feng, Z. Wu, Q. Wu, S. S. Park, C.-S. Ha and D. Zhao, Facile synthesis of porous carbon nitride spheres with hierarchical three-dimensional mesostructures for CO<sub>2</sub> capture, *Nano Res.*, 2010, **3**, 632–642.
- 60 D. Lin-Vien, N. B. Colthup, W. G. Fateley and J. G. Grasselli, *The Handbook of Infrared and Raman Characteristic Frequencies of Organic Molecules*, Elsevier Science, 1991.
- 61 W. Zhao, L. Luo, T. Chen, Z. Li, Z. Zhang, H. Wang, J. Rao, L. Feo and M. Fan, Synthesis and characterization of Pt-N-doped activated biocarbon composites for hydrogen storage, *Composites, Part B*, 2019, **161**, 464–472.
- 62 Z. Weigang, Hydrothermal doping of nitrogen in bamboo-based super activated carbon for hydrogen storage, *Bioresources*, 2017, **12**, 6237–6250.
- 63 Z. Wang, L. Sun, F. Xu, H. Zhou, X. Peng, D. Sun, J. Wang and Y. Du, Nitrogen-doped porous carbons with high performance for hydrogen storage, *Int. J. Hydrogen Energy*, 2016, **41**, 8489–8497.
- 64 N. Bader and O. Abdelmottaleb, CO<sub>2</sub> activation of olive bagasse for hydrogen storage, *Environ. Prog. Sustainable Energy*, 2017, **36**, 315–324.
- 65 S. H. Md Arshad, N. Ngadi, A. A. Aziz, N. S. Amin, M. Jusoh and S. Wong, Preparation of activated carbon from empty fruit bunch for hydrogen storage, *J. Energy Storage*, 2016, **8**, 257–261.
- 66 N. T. Mandoki, J. Dentzer, T. Piquero, S. Saadallah, P. David and C. Vix-Guterl, Hydrogen storage in activated carbon materials: role of the nanoporous texture, *Carbon*, 2004, **42**, 2744–2747.
- 67 E. Ustinov, H. Tanaka and M. Miyahara, Low-temperature hydrogen-graphite system revisited: experimental study and Monte Carlo simulation, *J. Chem. Phys.*, 2019, **151**, 024704.
- 68 Z. W. Zhu, Q. R. Zheng, Z. H. Wang, Z. Tang and W. Chen, Hydrogen adsorption on graphene sheets and nonporous graphitized thermal carbon black at low surface coverage, *Int. J. Hydrogen Energy*, 2017, **42**, 18465–18472.

